Room-Temperature Negative Differential Resistance in Surface-Supported Metal-Organic Framework Vertical Heterojunctions

*Luiz G. S. Albano, Davi H. S. de Camargo, Gabriel R. Schleder, Samantha G. Deeke, Tatiana P. Vello, Leirson D. Palermo, Cátia C. Corrêa, Adalberto Fazzio, Christof Wöll, and Carlos C. B. Bufon**

The advances of surface-supported metal-organic framework (SURMOF) thin-film synthesis have provided a novel strategy for effectively integrating metal-organic framework (MOF) structures into electronic devices. The considerable potential of SURMOFs for electronics results from their low cost, high versatility, and good mechanical flexibility. Here, the first observation of room-temperature negative differential resistance (NDR) in SURMOF vertical heterojunctions is reported. By employing the rolled-up nanomembrane approach, highly porous sub-15 nm thick HKUST-1 films are integrated into a functional device. The NDR is tailored by precisely controlling the relative humidity (RH) around the device and the applied electric field. The peak-to-valley current ratio (PVCR) of about two is obtained for low voltages (<2 V). A transition from a metastable state to a field emission-like tunneling is responsible for the NDR effect. The results are interpreted through band diagram analysis, density functional theory (DFT) calculations, and ab initio molecular dynamics simulations for quasisaturated water conditions. Furthermore, a low-voltage ternary inverter as a multivalued logic (MVL) application is demonstrated. These findings point out new advances in employing unprecedented physical effects in SURMOF heterojunctions, projecting these hybrid structures toward the future generation of scalable functional devices.

1. Introduction

Surface-supported metal-organic frameworks (SURMOFs) are a special form of metal-organic frameworks (MOFs), a huge class of hybrid and crystalline materials composed of metallic clusters connected by organic linkers. SURMOFs are grown on functionalized surfaces using a layer-by-layer process.[1] The SURMOF approach provides highly orientated, monolithic, and homogenous MOF films with adjustable thickness firmly grafted to desired surfaces,[2] thus outperforming other forms of MOF thin films. SURMOFs have good mechanical flexibility,[3] high versatility, and are well suited for integration into devices and systems in various application fields.[4,5] In particular, these structures opened new perspectives for the realization of novel electronic devices, e.g., as resistive switchers,[6–9] field-effect transistors,[10] and optoelectronics.[11–14] Despite these interesting advances, the full potential of this class of hybrid materials has not yet been fully explored, e.g., quantum electronic tunneling phenomena, which may lead to negative differential resistance (NDR), have not been reported for SURMOF-based devices. NDR requires a non-linear relation between current and voltage that results in a negative slope.[15] This effect is very beneficial for various applications, e.g., in resonators, oscillators, amplifiers, and logical devices, to mention a few. In resonators, NDR can cancel the internal losses, resulting in circuits with no damping.[16] For oscillators and amplifiers, the effect is

Dr. L. G. S. Albano, D. H. S. de Camargo, G. R. Schleder, S. G. Deeke, T. P. Vello, L. D. Palermo, Dr. C. C. Corrêa, Prof. A. Fazzio, Prof. C. C. B. Bufon
Brazilian Nanotechnology National Laboratory (LNNano)
Brazilian Center for Research in Energy and Materials (CNPEM)
Campinas, São Paulo 13083-970, Brazil
E-mail: carlos.bufon@lnnano.cnpem.br

D. H. S. de Camargo, S. G. Deeke, Prof. C. C. B. Bufon
Postgraduate Program in Materials Science and Technology (POSMAT)
São Paulo State University (UNESP)
Bauru, São Paulo 17033-360, Brazil

G. R. Schleder, Prof. A. Fazzio
Federal University of ABC (UFABC)
Santo André, São Paulo 09210-580, Brazil

T. P. Vello, Prof. C. C. B. Bufon
Department of Physical Chemistry
Institute of Chemistry (IQ)
University of Campinas (UNICAMP)
Campinas, São Paulo 13084-862, Brazil

Prof. C. Wöll
Institute of Functional Interfaces (IFG)
Karlsruhe Institute of Technology (KIT)
76344 Eggenstein-Leopoldshafen, Germany

responsible for converting the input DC to output AC signals. It can also be used to amplify an existing AC signal applied at the same terminals.[16] In the context of multivalued logic (MVL) applications, NDR can be employed to create additional logic states with less complexity. This feature minimizes power dissipation by reducing the number of devices on a circuit and bringing down the number of complicated interconnect lines (and their respective parasitic capacitance effects).[17,18]

Well-known devices utilizing NDR are Esaki and resonant tunneling diodes, mainly based on Si-Ge junctions and III-V semiconductors.[19–21] Nevertheless, these materials have limitations due to the lattice mismatch during their growth.[22,23] The NDR has also been observed in a variety of molecular and mesoscopic systems, including molecular junctions,[24] nanoparticles,[25] oxides,[26] hybrid systems,[27,28] graphene devices,[29] and van der Waals (vdW) heterostructures based on atomically 2D materials.[17,30–36] However, for some of these materials, in particular 2D materials, device integration is a challenging problem since issues related to the interface with contact electrodes,[37] and the difficulties in transferring and stacking them on target substrates severely complicates production on a larger scale.[38] Thus, the need for scalable and integrable hybrid materials to boost new electronics at low cost and to use standard fabrication processes is rather pressing. SURMOFs are promising materials in this context since the layer-by-layer deposition is fully compatible with many manufacturing processes. It ensures precise control of the thickness at the molecular scale onto the device's surface.[4,5] Furthermore, the electrical properties of these crystalline and porous thin films can be further modified by loading guest molecules and ions inside the pores.[6,11,39,40]

The NDR has also been reported in DMAMnF crystals (a multiferroic MOF), where peak-to-valley current ratio (PVCR) of about 10 have been reported for reduced temperatures (176 K).[41] However, the low-temperature operation and the difficult-to-integrate architecture based on bulk crystals compromise the device's application. HKUST-1 (Hong Kong University of Science and Technology) is a widely explored MOF that is well suited for the layer-by-layer process, allowing the growth of high-quality SURMOF films at ambient conditions a large variety of solid substrates.[2] The electronic structure of HKUST-1 SURMOF is susceptible to the presence of water, causing the appearance of additional states in the bandgap region.[6] Thus, by adequately tailoring external conditioning parameters, the band-structure of HKUST-1 SURMOFs can be designed to explore unprecedented quantum electronic tunneling phenomena.

Here we report the first observation of room-temperature NDR in HKUST-1 SURMOF vertical heterojunctions. The device structure relies on rolled-up metallic nanomembrane, which allows soft contacting the sub-15 nm thick HKUST-1 layer from the top. By precisely controlling the relative humidity (RH) around the device and the applied electric field, the NDR appears at low voltages (less than 2 V) with PVCR of about 2. The underlying physical mechanism is understood through band diagram analysis, density functional theory (DFT) calculations, and ab initio molecular dynamics simulations for quasisaturated water conditions. The potential of the SURMOF-based NDR device is demonstrated by realizing a typical MVL application, a low-voltage ternary inverter. These results show that by effectively controlling the experimental conditions in a suitable manufacturing platform, SURMOFs allow the exploitation of exciting quantum electronic effects to realize novel devices.

2. Results and Discussion

Figure 1a,b sketches the device architecture based on rolled-up metallic nanomembranes that yield well-defined and ultrathin HKUST-1 vertical heterojunctions. The HKUST-1 layer was grown using a layer-by-layer process on a finger-like electrode. The strained metallic nanomembrane (made of Au) provides a top mechanical contact after its strain gradient relaxation caused by dissolution of the sacrificial layer. The whole device fabrication involves conventional photolithography and thin film deposition, as shown in Figure S1 in the Supporting Information. Figure 1c shows the laser scanning confocal microscopy (LSCM) image of a single device with the bias configuration for electrical characterization. The grounded contacting pad was electrically connected to the finger-like (bottom) electrode, while the external contacting pads to the microtube-like (top) electrode. This device layout is scalable and provides a high integration density of 32 fabricated devices on a microchip containing 81 mm^2 of area (corresponding to 10^5 devices m^{-2}), as shown in Figure 1d and Figures S2 and S3 (Supporting Information).

In Figure 1e, an LSCM image of the active device area (dotted region from Figure 1c) is presented in detail. The top contact realized by the microtube results in different geometric and effective device contacting areas (A_{GEO} and A_{EFF}) of about 8 μm^2 and 10^3 nm^2,[6] respectively. These values are expected considering the soft and self-adjusted nature of the rolled-up nanomembrane and the involved interfaces' topography. The step-by-step HKUST-1 growth was performed as described earlier.[1,2] The grazing incidence X-ray diffraction (GIXRD) pattern shown in Figure 1f and Figure S4 (Supporting Information) reveals the presence of crystalline HKUST-1 thin films.[1,2,6] Well-orientated HKUST-1 films have been reported on COOH-terminated organic surfaces.[42,43] However, the two preferential orientations seen in Figure 1f and Figure S4 (Supporting Information) are consequences of the short-chain length from the SAM layer (6-mercaptohexanoic acid) and the low SURMOF thickness.[2] The atomic force microscopy (AFM) topography image, recorded after 15 layer-by-layer deposition cycles, is presented in Figure 1g. The image corresponds to the dotted region from Figure 1e – on the interface between the finger-like electrode and the patterned HKUST-1 layer. The SURMOF was patterned using photolithography processes that do not affect its integrity.[6] As can be seen, the monolithic HKUST-1 film is pinhole-free, and the surface roughness is low, with a root-mean-square (R_q) value of 4.91 ± 0.56 nm. The thickness amounts to around 15 nm.

The NDR behavior of the fabricated vertical heterojunctions is only observed after the Au/SAM-HKUST-1/Au sandwich structure is subjected to a conditioning process consisting of a sequential series of voltage sweeps under a high RH (90%) atmosphere. The voltage range for each conditioning sweep and

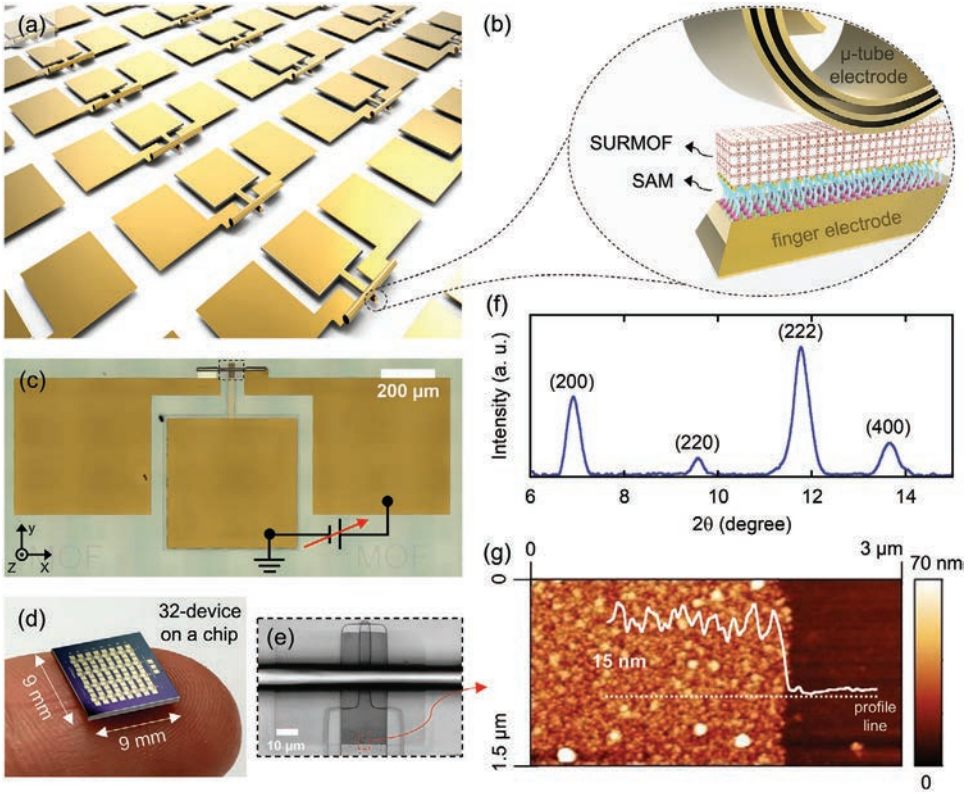

Figure 1. a,b) Illustration of an array of devices and the respective cross-sectional view (Au/SAM-HKUST-1/Au). c) LSCM image from a single device with the bias configuration for electrical measurements. d) Image of a microchip containing 32 devices. e) LSCM image from the dotted region in (c), showing the active device area in detail. f) GIXRD pattern for HKUST-1. g) AFM topography image from the dotted region in (e) and the respective profile thickness for HKUST-1.

the respective current outputs are shown in Figure S5 in the Supporting Information. During the final voltage sweep (0 to −2.5 V), **Figure 2a**, the output current abruptly increases from −2.1 V. This specific potential corresponds to an electric field of about ≈1.4 MV cm^{-1} across the vertical heterojunction. The subsequent *I*–*V* region is highlighted as the forming region. In Figure 2b, where the Fowler-Nordheim plot for the final voltage sweep is presented (in modulus), an inflection point can be observed, indicating a transition from the metastable condition to field emission-like (FE) tunneling. In general, for metal/insulator/metal junctions, the barrier shape changes from rectangular to triangular once the applied bias is higher than the energy barrier height.[44,45] The relation between the applied voltage and the current in such a regime can be described by Equation (1)

$$I_{FN} \propto V^2 \exp\left(-\frac{8\pi d\sqrt{2m^*\varphi^3}}{3h\epsilon V}\right) \quad (1)$$

where d, m^*, φ, and h are the tunneling thickness, effective electron mass, tunneling barrier height, and the Planck constant.

From the threshold voltage (V_{th}) obtained in Figure 2b, the tunneling barrier can be determined and amounts to ≈0.60 eV. According to the electrical characteristics, a simple schematic band diagram based on the FE tunneling can be deduced, as shown in the inset of Figure 2b. The inset (i) shows the band diagram for a positive applied voltage. The energy barrier (Φ) at the finger/SAM-HKUST-1 interface is substantially higher for electron injection. This explains the low values of output current. Under negative applied voltage, because of the absence of the SAM on the top electrode, the injection of electrons is favored. The electric field's continuous increase at this bias configuration changes the barrier width, making the tunneling probability for electrons proportional to the applied voltage, see inset (ii). After the conditioning process, which has the beginning of the FE tunneling regime as the control parameter, the current profile at positive applied voltages gradually increases, followed by observing the NDR behavior, as expressed by Equation (2)

$$r_{diff} = \frac{\Delta_v}{\Delta_i} < 0 \quad (2)$$

$$PVCR = \frac{I_{peak}}{I_{valley}} \quad (3)$$

where Δ_v and Δ_i are the variations between peak-to-valley voltage and the respective current in the NDR region, I_{peak} and I_{valley} are the peak and valley currents.

The typical NDR behavior obtained is presented in Figure 2c. By using Equation (3), a PVCR of around 2 was obtained at room temperature. The PVCR reaches good stability at the 5th *I*–*V* cycle after the conditioning process, as shown in Figure S6

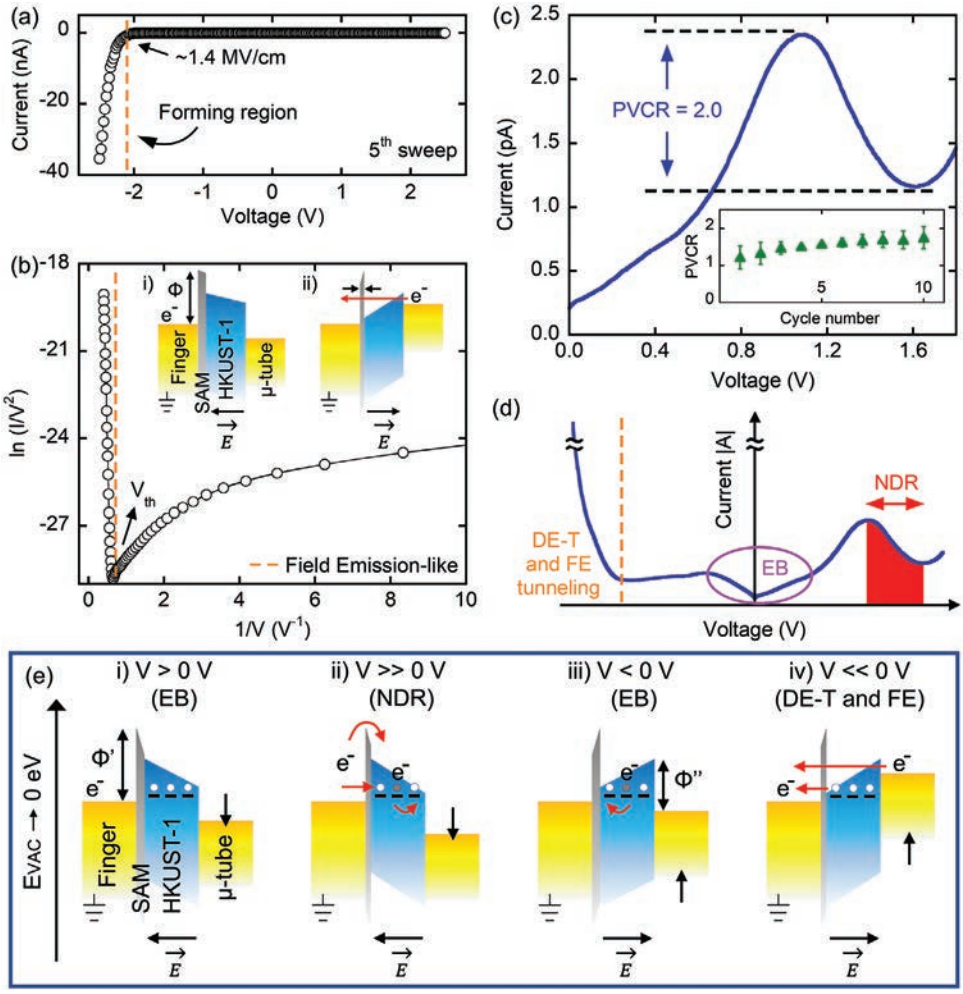

Figure 2. a) 5th conditioning sweep at 90% RH for the NDR creation in the Au/SAM-HKUST-1/Au vertical heterojunction. b) Typical Fowler-Nordheim plot for the negative applied voltages of the 5th conditioning sweep, indicating the transition from the metastable condition to FE tunneling (in modulus). The inset shows the schematic energy band diagrams for i) positive and ii) negative applied voltages bias, where the transition occurs. c) The NDR behavior at 90% RH after the conditioning process. (inset) PVCR as a function of the number of *I–V* cycles for different devices. d) Qualitative explanation of the *I–V* characteristics under different applied voltage conditions after the conditioning process. e) Schematic energy band diagrams for explaining (d).

in the Supporting Information. The NDR behavior appears at a positive applied voltage every time a negative cycle is performed (see Figure S7 in the Supporting Information). Therefore, the NDR behavior can be set-reset by inverting the voltage bias, creating a set-read combination. The inset of Figure 2c shows the PVCR values over the successive *I–V* cycles for different devices. Figure S8 in the Supporting Information shows the NDR for different devices.

The qualitative explanation of the *I–V* characteristics after the conditioning process is presented in Figure 2d. As mentioned, the energy barriers (here defined by EB) on both metal interfaces are asymmetric because between the finger-like electrode and the HKUST-1, there is the SAM layer. Regardless of the asymmetry, EB suppresses the output current for both bias configurations at low applied voltages. By increasing the electric field, the NDR behavior takes place for the positive applied voltages. By reversing the bias above EB, the output current achieves a plateau-like flowed of an increase as the electric field rises. This increase of the output current is a necessary condition to observe NDR in the following *I–V* cycle. This behavior can be interpreted as a de-trapping-like (DE-T) process,[46] although the possibility of FE tunneling cannot be ruled out. In Figure 2e, schematic energy band diagrams are presented. The effect of water molecules for inducing additional mid-gap states in HKUST-1 band-structure is considered as well.[6] Following the *I–V* characteristics in Figure 2d, after the conditioning process, Φ becomes Φ', as shown in the band diagram (i) from Figure 2e. Even under a change, Φ' is high enough to suppress the electron injection for small positive applied voltages. However, as shown in the band diagram (ii), by further increasing the positive applied voltage, the water-induced energy states in the HKUST-1 band-structure get filled (trapped), decreasing the output current and leading to the NDR behavior. There is also a certain probability of charge transfer across EB to the water-induced energy states via direct tunneling.[45] In the band diagram (iii), for $V < 0$ V, Φ'' is correlated to EB formed at

microtube/HKUST-1 interface – it also limits the electron injection. The plateau-like current profile is associated with the trap hopping-like process inside the HKUST-1 band-structure owing to the increased electric field. As the negative applied voltage increases, DE-T and FE processes occur, as shown in the band diagram (iv). These processes can be sequentially repeated as the *I*–*V* cycles evolve.

In addition to the band diagram analysis, to better understand the origin of the NDR behavior observed in Figure 2c, DFT calculations and ab initio molecular dynamics simulations were performed focusing on the interaction between water molecules and HKUST-1 unit cell with structural defects. Previous experimental work has demonstrated that structural defects (i.e., Cu^{+} species) with concentrations up to 2% are present in as-grown HKUST-1.[47] The relation between the electronic properties and the atomic configurations under different scenarios is evaluated next. **Figure 3a**–d and Figure S9 (Supporting Information) show the electronic element-projected density of states (pDOS) for HKUST-1 in distinct conditions. Perfect, fully stoichiometric HKUST-1 is a good insulator, with a fully occupied valence band composed mainly of O-orbitals and an empty conduction band, which mostly involves Cu-orbitals (Figure 3a). Note that the theoretical band gap (1.83 eV) is substantially smaller than the experimental one, 3.6 eV.[48] This underestimate of the bandgap is a well-known shortcoming of the DFT approximations.[6] In the ideal structure, all Cu centers have an approximate atomic charge of +1 (Table S1, Supporting Information), which corresponds to the Cu^{2+} species. The interpretation between ion oxidation states and DFT atomic charges is not straightforward. It relies on the model or theory employed to handle the electron density around atomic centers, although its numerical trend has the utility to elucidate chemical processes.[49,50] Thus, we proceeded by investigating the effect of such oxygen vacancies, which are responsible for introducing mid-gap defect levels with a small density of states (see Figure S9a,b in the Supporting Information). Furthermore,

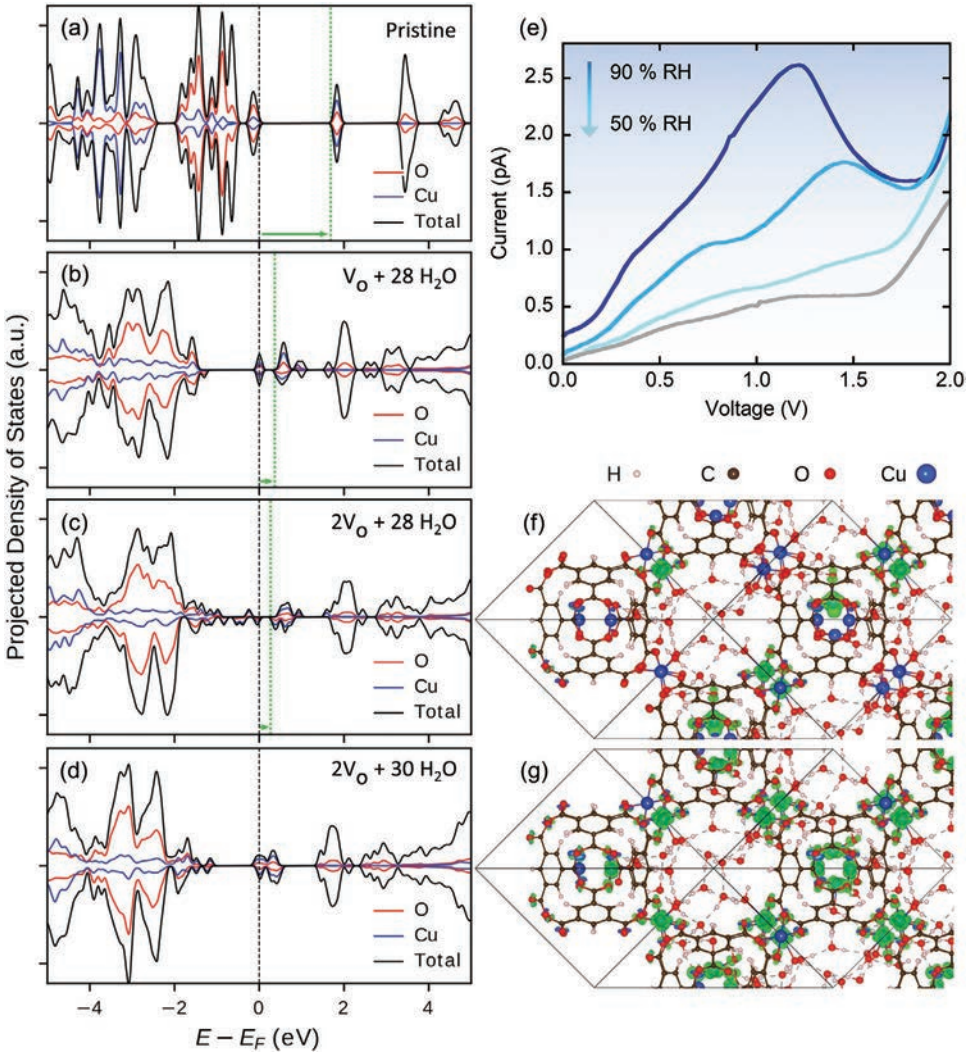

Figure 3. a–d) pDOS for HKUST-1 under different conditions. The arrow pointing to the green dashed lines indicates the Cu states' energy related to the Fermi level (black dashed lines). Positive and negative values represent majority and minority spin contributions. e) NDR behavior experimentally obtained at different RHs. f,g) Real-space representation (in green) of the charge density ($\rho(\boldsymbol{r}) = e|\psi(\boldsymbol{r})|^2$) of energy states near (± 0.5 eV) to the Fermi level for the conditions in (c) and (d), respectively. Isosurface value of 0.01 e^{-} $Å^{-3}$.

the Cu atomic charge is reduced by –0.3 compared with the pristine condition (see Table S1 in the Supporting Information).

The simulated experimental humidity conditions are set by placing a spherical box of liquid water containing 28 water molecules in the hydrophilic HKUST-1 pore.[51,52] This specific number was estimated from the number of molecules that would fit within the pore volume. Such a volume corresponds to the approximate experimental condition where RH value is 90% (Figure S10, Supporting Information). Next, short ab initio molecular dynamics simulations were performed at 300 K to study the interaction between water molecules and the open Cu sites. We observe that the water molecules near the Cu centers are physisorbed with a vertical orientation, while the other molecules form a hydrogen-bonded network within the pore. When one or more water molecules interact with the defective Cu site, the pDOS of the defect-mid-gap states increases, as shown in Figure 3b and Figure S9c,d (Supporting Information). The RH, as simulated by the number of water molecules inside the HKUST-1 pore, can thus effectively modulate the Fermi energy, acting as an electron donor. An additional oxygen vacancy at the Cu atom, adjacent to the first defective center (corresponding now to a carboxylate vacancy), leads to several localized defect states below the Fermi level (Figure 3c; Figure S9e, Supporting Information). The carboxylate vacancy is the structural defect that correlates with experimental findings.[47] In this scenario, a small bandgap of about 0.32 eV still exists. Interestingly, each Cu center has a different atomic charge state, one with increased and another with approximately equal electron density compared to the pristine case (Table S1, Supporting Information), consistent with the recent identification of Cu^{+} and Cu^{2+} ions.[47]

Finally, by including two additional water molecules interacting with the defective Cu center, the local environment resembles the coordination with four oxygens (Figure S9f, Supporting Information). The defect/water levels exhibit better-defined energies instead of scattered values around the pristine bandgap, Figure 3d. Combined with the Fermi level shift caused by the water doping effect, in the new system configuration, Cu energy states (corresponding to the conduction band of the pristine condition) are now occupied. This result implies that electronic states are well-delocalized along with the structure, forming conducting channels. Figure 3e shows the NDR behavior experimentally obtained at different values of RH. For RH ≤ 70%, the NDR disappears. Such a condition corresponds to approximately 22 molecules of water inside of the HKUST-1 pore, as shown in Figure S10 in the Supporting Information. Furthermore, a sharp drop of about 40% in NDR performance is observed for 80% RH, possibly associated with the non-delocalization of water-based defect states. The complete set of *I*–*V* traces are presented in Figures S11 and S12 in the Supporting Information. The formation of conducting channels inside the pores can be better visualized in the real-space representation of the charge density ($\rho(\boldsymbol{r}) = e|\psi(\boldsymbol{r})|^2$) of the energy states near (± 0.5 eV) to the Fermi level. Figure 3f,g (and Figure S9e,f in the Supporting Information) shows the representation for 28 and 30 water molecules, respectively. In the first case, water-based defect states are localized, while in the latter case, the states are delocalized over several Cu centers. Therefore, under an electric field, such states can be loaded and unloaded, which will then mediate the electronic conductivity modulation by accessing a higher number of Cu delocalized states. The experimental results correlate with the DFT calculations and ab initio molecular dynamics simulations, suggesting that 90% RH is optimal for achieving the best NDR performance in the present HKUST-1 SURMOF vertical heterojunctions.

After performing the DFT calculations and ab initio molecular dynamics simulations, the NDR effect was employed to realize a ternary inverter. This type of device is considered a fundamental building block in MVL applications. **Figure 4a** shows the equivalent circuit configuration of the device assembly. The SURMOF vertical heterojunction (SURMOF NDR device) was connected in series with a bottom-contact copper (II) phthalocyanine (CuPc) Organic Field-Effect Transistor (OFET). In this circuit, the SURMOF NDR device acts as a driver element, while the CuPc OFET is a load resistor. The input voltage (V_{IN}) was applied to the bottom-gate, while the supply voltage (V_{DD}) to CuPc OFET drain electrode. The finger-like contact in the NDR device is grounded (V_{SS}). The output voltage (V_{OUT}) is the channel between the NDR and OFET devices. Figure 4b shows optical microscopy images of both devices; the connections that configure the circuit were performed by tungsten tips using micromanipulators. Further integration is also possible. The optical microscopy image showing the CuPc OFET in detail and its overall performance are presented in Figures S13 and S14 in the Supporting Information.

The V_{IN} versus V_{OUT} characteristic curve is shown in Figure 4c. By varying V_{IN} from 1.9 to 1.4 V at a fixed V_{DD} = 2.0 V, three well-defined logical states appear: i) V_{OUT} < 0.3 V for 1.9 V > V_{IN} > 1.8 V (logical state "0"), ii) 1.2 < V_{OUT} < 1.7 V for 1.65 V > V_{IN} > 1.55 V (logic state "1"), and iii) V_{OUT} > 1.8 V for 1.5 V > V_{IN} > 1.4 V (logical state "2"). The inset in Figure 4c shows the respective input-output table, indicating how the three logical states change as a function of V_{IN} and V_{OUT}. Figure 4d shows the voltage-transfer characteristics of the CuPc OFET with the same applied voltages employed in the ternary inverter circuit. The output current (I_{DS}) with very low hysteresis is close to the current observed in the NDR behavior for 1.65 V > V_{GS} > 1.55 V. The low leakage current (I_{GS}) at these conditions is presented in Figure S15 in the Supporting Information. In the sequence, to solidify the proof-of-concept, we replaced the SURMOF NDR device in the circuit by a vertical heterojunction without the NDR effect (Figure S16a, Supporting Information), i.e., which was not submitted to the conditioning process. As shown in Figure S16b in the Supporting Information, only two logical states were observed ("0" and "1"), both associated with the CuPc OFET operation. To better understand the functioning of this circuit, we proceed by analyzing the CuPc OFET characteristics and performing load-line circuit analysis. This analysis is based on the intersections of the two characteristic curves that properly identify the circuit's operating points. As can be seen in Figure 4e, for 1.9 V > V_{IN} > 1.8 V, the load resistor (CuPc OFET) is turned off, which provided a high-resistance path in the channel region, resulting in low voltage values at the output terminal (red circles, logic state "0"). For 1.65 V > V_{IN} > 1.55 V, a moderate-resistance level is set in the channel region. In this condition, the operating points sit in the peak and valley NDR regions (blue circles, logic state "1"), Figure 4e. By decreasing V_{IN} (<1.5 V), the load resistor provides a low-resistance path

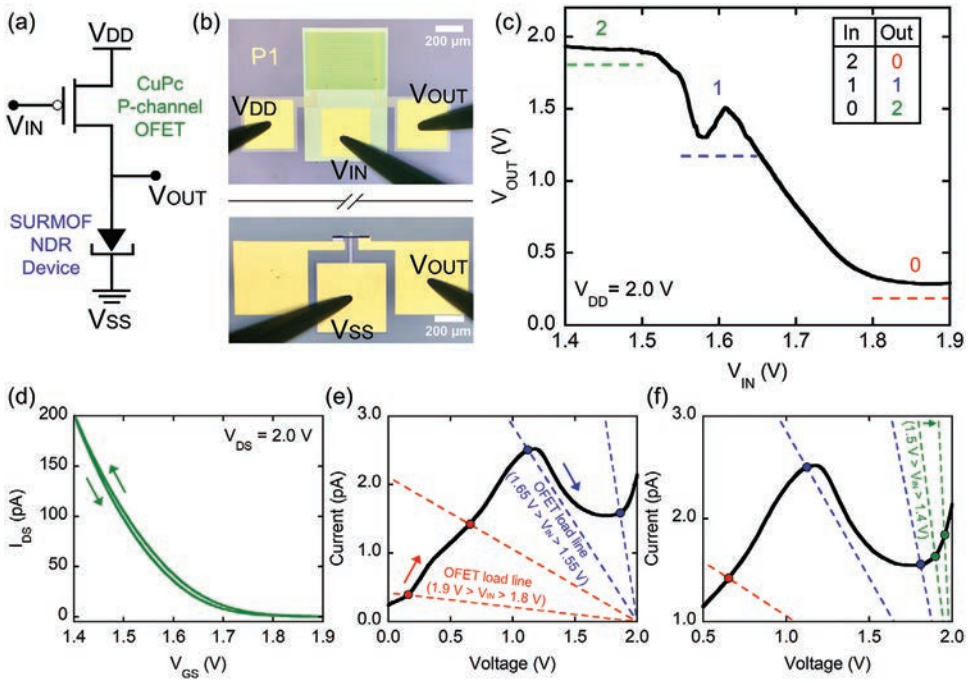

Figure 4. a) Equivalent circuit for the ternary inverter. b) Optical microscopy images showing the connection between the CuPc OFET and SURMOF vertical heterojunction (SURMOF NDR device) creating a ternary inverter. c) V_{IN} versus V_{OUT} characteristic curve of the ternary inverter – (inset) respective input-output table. d) Voltage-transfer characteristics for the CuPc OFET at the same applied voltages employed in the ternary inverter circuit. e,f) Load-line analysis of the ternary inverter circuit for the three distinct logical states obtained ("0," "1," and "2"). The solid and dashed lines represent the SURMOF NDR device (driver) and the CuPc OFET (load resistor).

because the CuPc OFET turns on. In this condition, the output voltage measured is close to V_{DD}, corresponding to the logic state "2," green circles in Figure 4f.

3. Conclusion

In summary, we report the first observation of the NDR effect in ultrathin SURMOF vertical heterojunctions at room temperature and low operation voltages. Using an integrated fabrication approach based on strained nanomembranes and a conditioning process, reproducible devices show the NDR effect with PVCRs around 2. A transition from the metastable condition to FE tunneling provides access to a finite number of water-defect states near the HKUST-1 Fermi level, which is interpreted using DFT calculations and ab initio molecular dynamics simulations. This work also demonstrates that defect engineering can be a powerful way to tune the electronic properties of SURMOF thin-film devices. Furthermore, the NDR effect is exploited to realize a low-voltage ternary inverter, a prototype MVL device. By adequately controlling V_{IN} and V_{DD}, V_{OUT} displays three distinct logic states ("0," "1," and "2"). This work projects SURMOF thin-film structures toward the future generation of scalable functional devices and logic circuits.

4. Experimental Section

Device Fabrication: Au/SAM-HKUST-1/Au vertical heterojunctions were fabricated on 9 mm x 9 mm conductive (100) silicon wafers covered with a 2 µm thick SiO_2 layer, following the approach described previously.[6] The detailed fabrication steps are depicted in Figure S1 in the Supporting Information. The CuPc OFETs were fabricated on 12 mm x 12 mm conductive (100) silicon wafers covered with a 2 µm thick SiO_2 layer. The fabrication was performed using conventional photolithography with AZ 5214E photoresist for patterning and e-beam evaporation (10^{-7} Torr, room temperature) for metallic deposition. First, the bottom-gate electrode was created by patterning and depositing 20 nm of Cr at 1 Å s^{-1}. Then, 20 nm of Al_2O_3 gate dielectric was deposited through thermal atomic layer deposition (ALD) at 150 °C using trimethylaluminum (TMA) and water precursors. This Al_2O_3 insulator layer covered the entire substrate surface, including the bottom-gate electrode. By proceeding with device fabrication, the source-drain electrodes were patterned to create an interdigitated region (channel region) containing a W/L ratio of 1000, where L = 10 µm (distance between source-drain electrodes in the channel region). Then, a bilayer composed of Cr/Au (5/5 nm) was deposited both at 0.4 Å s^{-1}. Next in the sequence, the contacting-pads of source, gate, and drain electrodes were patterned, followed by a reactive ion etching process using O_2 to access the bottom-gate electrode. Then, the contacting-pads Cr/Au (20/40 nm) were deposited both at 0.5 Å s^{-1}. Finally, the channel region was patterned, followed by the thermal sublimation of 20 nm CuPc layer at 0.3 Å s^{-1} in a vacuum condition (10^{-6} Torr) to form the semiconducting OFET channel. After all fabrication processes were completed, CuPc OFETs were kept 24 h in a vacuum before characterization.

Characterization: LSCM images of the SURMOF vertical heterojunctions were collected using a VK-X200 microscope from Keyence (USA). GIXRD patterns of HKUST-1 SURMOF were acquired using the XRD2 beamline from the Brazilian Synchrotron Light Laboratory (LNLS), with an incident wavelength (λ) 1.54979 Å equipped with a Mythen linear detector for spectra acquisition. AFM topography images were obtained with a Park NX10 AFM microscope and treated using Gwyddion software. The electrical characteristics were measured using a Semiconductor Parameter Analyzer 4200-SCS from Keithley

(USA) with a limit of electrical current of 10^{-15} A. For NDR investigation, the number of voltage steps was kept fixed to 0.2 V for all curves, and the electrical current was measured using the quiet integration mode. The electrical connections between the vertical heterojunctions and OFETs, including the logical circuit, were performed through micromanipulators with tungsten tips coupled with a conventional optical microscope. It is worth mention that the integration of both devices on a chip is feasible. Triaxial connectors were used, connecting the micromanipulators to the SCS. The SURMOF vertical heterojunctions were measured in a homemade chamber with controlled RH, and the CuPc OFETs were measured in an inert atmosphere.

Theoretical Calculations: DFT calculations were performed within the generalized-gradient approximation as parametrized by Perdew-Burke-Ernzerhof (GGA-PBE) for the exchange-correlation functional [53–55] using the projector-augmented-wave (PAW) method,[56,57] implemented in the VASP software package.[58] The energy cutoff of 400 eV was used for the plane-wave expansion and a Hubbard U parameter of 5 eV for Cu d orbitals [59] according to previous studies.[6] A relaxed triclinic unit cell (a = 18.739 Å, $\alpha = 60°$) was used with an initial antiferromagnetic coupling for the Cu pairs in the MOF structure. All configurations were relaxed using Γ-only k-space sampling with a force threshold of 10^{-2} eV $Å^{-1}$. For the pDOS, a 4×4×4 Monkhorst-Pack Brillouin Zone k-point sampling was used. Ab initio molecular dynamics were performed using the SIESTA DFT package with norm-conserving pseudopotentials and polarized double-ζ (DZP) basis-set.[60,61] The canonical ensemble (NVT, constant number of particles *N*, volume *V*, and temperature *T*) was sampled by using a Nosé-Hoover thermostat at 300 K for 4 ps, with an integration time of 1 fs.

Acknowledgements

This work was supported by São Paulo Research Foundation (FAPESP) (Grants: 2014/25979-2, 2016/25346-5, 2017/25553-3, 2017/18139-6, 2017/02317-2, 2019/01561-2), and National Council for Scientific and Technological Development (CNPq) (Grant: 408770/2018-0). C.C.B.B. is a productivity research fellow from CNPq (Grants: 305305/2016-6, 306768/2019-4), and also acknowledge CNPq and FAPESP via the National Institute of Science and Technology in Functional Complex Materials (INCT)-INOMAT (CNPq, Grant: 465452/2014-0, FAPESP, Grant: 2014/50906-9). C.C.B.B. also acknowledges the Coordination for the Improvement of Higher Education Personnel (CAPES) and Alexander von Humboldt Foundation by Experienced Research Fellowship (CAPES, process 88881.145646/2017-01). This research used resources from Brazilian Synchrotron Light Laboratory (LNLS) (proposals: 20170812, 20180148, 20180742) and Brazilian Nanotechnology National Laboratory (LNNano) (proposals: AFM-24654, AFM-26354, AFM-27465), open facilities from Brazilian Center for Research in Energy and Materials (CNPEM). The authors also acknowledge the Santos Dumont supercomputer at the Brazilian National Scientific Computing Laboratory (LNCC) for computational resources.

Conflict of Interest

The authors declare no conflict of interest.

Data Availability Statement

Research data are not shared.

Keywords

metal-organic frameworks, multivalued logic applications, negative differential resistance, SURMOF diodes, ternary inverters

[1] O. Shekhah, H. Wang, S. Kowarik, F. Schreiber, M. Paulus, M. Tolan, C. Sternemann, F. Evers, D. Zacher, R. A. Fischer, C. Wöll, *J. Am. Chem. Soc.* **2007**, *129*, 15118.
[2] T. P. Vello, M. Strauss, C. A. R. Costa, C. C. Corrêa, C. C. B. Bufon, *Phys. Chem. Chem. Phys.* **2020**, *22*, 5839.
[3] J. H. Lee, S. Jeoung, Y. G. Chung, H. R. Moon, *Coord. Chem. Rev.* **2019**, *389*, 161.
[4] J. Liu, C. Wöll, *Chem. Soc. Rev.* **2017**, *46*, 5730.
[5] L. Heinke, C. Wöll, *Adv. Mater.* **2019**, *31*, 1806324.
[6] L. G. S. Albano, T. P. Vello, D. H. S. de Camargo, R. M. L. da Silva, A. C. M. Padilha, A. Fazzio, C. C. B. Bufon, *Nano Lett.* **2020**, *20*, 1080.
[7] X. Yi, Z. Yu, X. Niu, J. Shang, G. Mao, T. Yin, H. Yang, W. Xue, P. Dhanapal, S. Qu, G. Liu, R.-W. Li, *Adv. Electron. Mater.* **2019**, *5*, 1800655.
[8] Z. Wang, D. Nminibapiel, P. Shrestha, J. Liu, W. Guo, P. G. Weidler, H. Baumgart, C. Wöll, E. Redel, *ChemNanoMat* **2016**, *2*, 67.
[9] L. Pan, Z. Ji, X. Yi, X. Zhu, X. Chen, J. Shang, G. Liu, R.-W. Li, *Adv. Funct. Mater.* **2015**, *25*, 2677.
[10] Z.-G. Gu, S.-C. Chen, W.-Q. Fu, Q. Zheng, J. Zhang, *ACS Appl. Mater. Interfaces* **2017**, *9*, 7259.
[11] X. Liu, M. Kozlowska, T. Okkali, D. Wagner, T. Higashino, G. Brenner-Weiß, S. M. Marschner, Z. Fu, Q. Zhang, H. Imahori, S. Bräse, W. Wenzel, C. Wöll, L. Heinke, *Angew. Chem., Int. Ed.* **2019**, *58*, 9590.
[12] M. Oldenburg, A. Turshatov, D. Busko, S. Wollgarten, M. Adams, N. Baroni, A. Welle, E. Redel, C. Wöll, B. S. Richards, I. A. Howard, *Adv. Mater.* **2016**, *28*, 8477.
[13] J. Ou, J. Xiang, J. Liu, L. Sun, *ACS Appl. Mater. Interfaces* **2019**, *11*, 14862.
[14] Y.-B. Tian, Y.-Y. Wang, S.-M. Chen, Z.-G. Gu, J. Zhang, *ACS Appl. Mater. Interfaces* **2020**, *12*, 1078.
[15] L. Esaki, *Phys. Rev.* **1958**, *109*, 603.
[16] C. Poole, I. Darwazeh, *Microwave Active Circuit Analysis and Design*, Academic Press, Oxford, UK **2015**.
[17] J. Shim, S. Oh, D.-H. Kang, S.-H. Jo, M. H. Ali, W.-Y. Choi, K. Heo, J. Jeon, S. Lee, M. Kim, Y. J. Song, J.-H. Park, *Nat. Commun.* **2016**, *7*, 13413.
[18] S. L. Hurst, *IEEE Trans. Comput.* **1984**, *C-33*, 1160.
[19] N. Jin, S.-Y. Chung, R. M. Heyns, P. R. Berger, R. Yu, P. E. Thompson, S. L. Rommel, *IEEE Electron Device Lett.* **2004**, *25*, 646.
[20] K.-J. Gan, C.-S. Tsai, Y.-W. Chen, W.-K. Yeh, *Solid-State Electron.* **2010**, *54*, 1637.
[21] B. Ganjipour, A. W. Dey, B. M. Borg, M. Ek, M.-E. Pistol, K. A. Dick, L.-E. Wernersson, C. Thelander, *Nano Lett.* **2011**, *11*, 4222.
[22] M. Holland, M. van Dal, B. Duriez, R. Oxland, G. Vellianitis, G. Doornbos, A. Afzalian, T.-K. Chen, C.-H. Hsieh, P. Ramvall, T. Vasen, Y.-C. Yeo, M. Passlack, *Sci. Rep.* **2017**, *7*, 14632.
[23] M. Steidl, C. Koppka, L. Winterfeld, K. Peh, B. Galiana, O. Supplie, P. Kleinschmidt, E. Runge, T. Hannappel, *ACS Nano* **2017**, *11*, 8679.
[24] J. Liu, D. Segal, *Nano Lett.* **2020**, *20*, 6128.
[25] J. Zheng, J. Zhang, Z. Wang, L. Zhong, Y. Sun, Z. Liang, Y. Li, L. Jiang, X. Chen, L. Chi, *Adv. Mater.* **2018**, *30*, 1802731.
[26] S. Kumar, Z. Wang, N. Davila, N. Kumari, K. J. Norris, X. Huang, J. P. Strachan, D. Vine, A. L. D. Kilcoyne, Y. Nishi, R. S. Williams, *Nat. Commun.* **2017**, *8*, 658.

[27] W. Choi, S. Hong, Y. Jeong, Y. Cho, H. G. Shin, J. H. Park, Y. Yi, S. Im, *Adv. Funct. Mater.* **2021**, *31*, 2009436.
[28] K.-S. Jung, K. Heo, M.-J. Kim, M. Andreev, S. Seo, J.-O. Kim, J.-H. Lim, K.-H. Kim, S. Kim, K. S. Kim, G. Y. Yeom, J. H. Cho, J.-H. Park, *Adv. Sci.* **2020**, *7*, 2000991.
[29] P. Sharma, L. S. Bernard, A. Bazigos, A. Magrez, A. M. Ionescu, *ACS Nano* **2015**, *9*, 620.
[30] J. Shim, D.-H. Kang, Y. Kim, H. Kum, W. Kong, S.-H. Bae, I. Almansouri, K. Lee, J.-H. Park, J. Kim, *Carbon* **2018**, *133*, 78.
[31] K.-H. Kim, H.-Y. Park, J. Shim, G. Shin, M. Andreev, J. Koo, G. Yoo, K. Jung, K. Heo, Y. Lee, H.-Y. Yu, K. R. Kim, J. H. Cho, S. Lee, J.-H. Park, *Nanoscale Horiz.* **2020**, *5*, 654.
[32] Q. Lv, F. Yan, N. Mori, W. Zhu, C. Hu, Z. R. Kudrynskyi, Z. D. Kovalyuk, A. Patanè, K. Wang, *Adv. Funct. Mater.* **2020**, *30*, 1910713.
[33] J. Lee, N. T. Duong, S. Bang, C. Park, D. A. Nguyen, H. Jeon, J. Jang, H. M. Oh, M. S. Jeong, *Nano Lett.* **2020**, *20*, 2370.
[34] S. Fan, S. J. Yun, W. J. Yu, Y. H. Lee, *Adv. Sci.* **2020**, *7*, 1902751.
[35] S. Fan, Q. A. Vu, S. Lee, T. L. Phan, G. Han, Y.-M. Kim, W. J. Yu, Y. H. Lee, *ACS Nano* **2019**, *13*, 8193.
[36] X. Zhou, X. Hu, S. Zhou, H. Song, Q. Zhang, L. Pi, L. Li, H. Li, J. Lü, T. Zhai, *Adv. Mater.* **2018**, *30*, 1703286.
[37] D. S. Schulman, A. J. Arnold, S. Das, *Chem. Soc. Rev.* **2018**, *47*, 3037.
[38] C.-H. Lee, G.-H. Lee, A. M. van der Zande, W. Chen, Y. Li, M. Han, X. Cui, G. Arefe, C. Nuckolls, T. F. Heinz, J. Guo, J. Hone, P. Kim, *Nat. Nanotechnol.* **2014**, *9*, 676.
[39] J. Liu, T. Wächter, A. Irmler, P. G. Weidler, H. Gliemann, F. Pauly, V. Mugnaini, M. Zharnikov, C. Wöll, *ACS Appl. Mater. Interfaces* **2015**, *7*, 9824.
[40] L. Shen, H. B. Wu, F. Liu, J. L. Brosmer, G. Shen, X. Wang, J. I. Zink, Q. Xiao, M. Cai, G. Wang, Y. Lu, B. Dunn, *Adv. Mater.* **2018**, *30*, 1707476.
[41] V. Malik, S. Maity, R. Chatterjee, *Org. Electron.* **2018**, *56*, 5.
[42] Z.-G. Gu, A. Pfriem, S. Hamsch, H. Breitwieser, J. Wohlgemuth, L. Heinke, H. Gliemann, C. Wöll, *Microporous Mesoporous Mater.* **2015**, *211*, 82.
[43] Z. Chen, Z.-G. Gu, W.-Q. Fu, F. Wang, J. Zhang, *ACS Appl. Mater. Interfaces* **2016**, *8*, 28737.
[44] J. W. Gadzuk, E. W. Plummer, *Rev. Mod. Phys.* **1973**, *45*, 487.
[45] C. C. B. Bufon, J. D. A. Espinoza, D. J. Thurmer, M. Bauer, C. Deneke, U. Zschieschang, H. Klauk, O. G. Schmidt, *Nano Lett.* **2011**, *11*, 3727.
[46] G. Yang, C. H. Jia, Y. H. Chen, X. Chen, W. F. Zhang, *J. Appl. Phys.* **2014**, *115*, 204515.
[47] W. Wang, D. I. Sharapa, A. Chandresh, A. Nefedov, S. Heißler, L. Heinke, F. Studt, Y. Wang, C. Wöll, *Angew. Chem., Int. Ed.* **2020**, *59*, 10514.
[48] Z.-G. Gu, L. Heinke, C. Wöll, T. Neumann, W. Wenzel, Q. Li, K. Fink, O. D. Gordan, D. R. T. Zahn, *Appl. Phys. Lett.* **2015**, *107*, 183301.
[49] A. Walsh, A. A. Sokol, J. Buckeridge, D. O. Scanlon, C. R. A. Catlow, *J. Phys. Chem. Lett.* **2017**, *8*, 2074.
[50] A. Walsh, A. A. Sokol, J. Buckeridge, D. O. Scanlon, C. R. A. Catlow, *Nat. Mater.* **2018**, *17*, 958.
[51] J. Getzschmann, I. Senkovska, D. Wallacher, M. Tovar, D. Fairen-Jimenez, T. Düren, J. M. van Baten, R. Krishna, S. Kaskel, *Microporous Mesoporous Mater.* **2010**, *136*, 50.
[52] J. B. Souza Junior, G. R. Schleder, F. M. Colombari, M. A. de Farias, J. Bettini, M. van Heel, R. V. Portugal, A. Fazzio, E. R. Leite, *J. Phys. Chem. Lett.* **2020**, *11*, 1564.
[53] W. Kohn, *Rev. Mod. Phys.* **1999**, *71*, 1253.
[54] G. R. Schleder, A. C. M. Padilha, C. M. Acosta, M. Costa, A. Fazzio, *J. Phys. Mater.* **2019**, *2*, 032001.
[55] J. P. Perdew, K. Burke, M. Ernzerhof, *Phys. Rev. Lett.* **1996**, *77*, 3865.
[56] P. E. Blöchl, *Phys. Rev. B* **1994**, *50*, 17953.
[57] G. Kresse, D. Joubert, *Phys. Rev. B* **1999**, *59*, 1758.
[58] G. Kresse, J. Furthmüller, *Phys. Rev. B* **1996**, *54*, 11169.
[59] S. L. Dudarev, G. A. Botton, S. Y. Savrasov, C. J. Humphreys, A. P. Sutton, *Phys. Rev. B* **1998**, *57*, 1505.
[60] J. M. Soler, E. Artacho, J. D. Gale, A. García, J. Junquera, P. Ordejón, D. Sánchez-Portal, *J. Phys.: Condens. Matter* **2002**, *14*, 2745.
[61] M. J. van Setten, M. Giantomassi, E. Bousquet, M. J. Verstraete, D. R. Hamann, X. Gonze, G.-M. Rignanese, *Comput. Phys. Commun.* **2018**, *226*, 39.